OPEN

NPG Asia Materials (2016) 8, e294; doi:10.1038/am.2016.104
www.nature.com/am

ORIGINAL ARTICLE

Hierarchical urchin-shaped α-MnO_2 on graphene-coated carbon microfibers: a binder-free electrode for rechargeable aqueous Na–air battery

Ziyauddin Khan[1], Seungyoung Park[1], Soo Min Hwang, Juchan Yang, Youngsu Lee, Hyun-Kon Song, Youngsik Kim and Hyunhyub Ko

With the increasing demand of cost-effective and high-energy devices, sodium–air (Na–air) batteries have attracted immense interest due to the natural abundance of sodium in contrast to lithium. In particular, an aqueous Na–air battery has fundamental advantage over non-aqueous batteries due to the formation of highly water-soluble discharge product, which improve the overall performance of the system in terms of energy density, cyclic stability and round-trip efficiency. Despite these advantages, the rechargeability of aqueous Na–air batteries has not yet been demonstrated when using non-precious metal catalysts. In this work, we rationally synthesized a binder-free and robust electrode by directly growing urchin-shaped MnO_2 nanowires on porous reduced graphene oxide-coated carbon microfiber (MGC) mats and fabricated an aqueous Na–air cell using the MGC as an air electrode to demonstrate the rechargeability of an aqueous Na–air battery. The fabricated aqueous Na–air cell exhibited excellent rechargeability and rate capability with a low overpotential gap (0.7 V) and high round-trip efficiency (81%). We believe that our approach opens a new avenue for synthesizing robust and binder-free electrodes that can be utilized to build not only metal–air batteries but also other energy systems such as supercapacitors, metal–ion batteries and fuel cells.
NPG Asia Materials (2016) **8,** e294; doi:10.1038/am.2016.104; published online 22 July 2016

INTRODUCTION

A rechargeable metal–air battery can be designed by properly selecting and fabricating an air electrode, which is commonly composed of an electrocatalyst, a binder and a conductive substrate.[1,2] An efficient electrocatalyst should be bifunctional and robust in nature. A bifunctional electrocatalyst catalyzes both the oxygen reduction reaction (ORR) and the oxygen evolution reaction (OER) during the battery discharge–charge process.[3] Although noble metals such as Pt, Pd, Ru, Au and Ag display good catalytic activity towards the ORR and OER, their low abundance and high cost impede their scalability for practical applications.[4–6] In recent years, economically favorable transition metal oxide catalysts (such as MnO_2, Co_3O_4, Fe_3O_4 and their composites)[1,6–10] and carbon-based materials (such as carbon black, graphene and carbon nanotubes)[3,11–13] have attracted great attention as electrocatalysts for metal–air batteries. Among the transition metal oxides, MnO_2 has drawn particular attention as an electrocatalyst owing to its low cost, high abundance and excellent ORR and OER catalytic activities in alkaline media.[14,15] Graphene and its derivatives have also been recognized as efficient catalysts owing to their superior electronic conductivities, fast charge-transport mobilities and high specific surface areas.[16,17] In addition, graphene can be used as a catalyst support to enhance the stability of the catalyst because of its chemical and electrochemical stabilities.[18] Although both MnO_2 and graphene exhibit outstanding catalytic activities, no reports have been published on robust bifunctional air electrodes based on urchin-shaped MnO_2 grown on a graphene-coated conductive substrate (carbon microfiber is used) without the use of a binder. Although a binder is included to enhance the physical contact between the active material and the conductive substrate, it hinders the ion and electron transport in the system and thereby causes electrode polarization, which can result in a high-charge overpotential and a low round-trip efficiency. Moreover, the addition of a binder increases the weight of the electrode and requires the execution of additional steps to mix and combine the materials during the electrode preparation process.[19] Therefore, it is desirable to design and develop binder-free bifunctional electrodes that can be directly utilized for rechargeable metal–air batteries.

Herein, we rationally synthesized hierarchical urchin-shaped α-MnO_2 on reduced graphene oxide (rGO) -coated carbon microfiber (MGC) and studied the rechargeability of a sodium–air (Na–air) battery in aqueous (mixed aqueous/aprotic) electrolyte with air as the oxygen source. Na–air batteries have recently emerged as alternatives to lithium–air batteries owing to their high abundance, low cost, safety and environmental friendliness.[20–24] Depending on the electrolyte,

School of Energy and Chemical Engineering, Ulsan National Institute of Science and Technology (UNIST), Ulsan, Republic of Korea
[1]These authors contributed equally to this work.
Correspondence: Professor Y Kim or Professor H Ko, School of Energy and Chemical Engineering, Ulsan National Institute of Science and Technology (UNIST), UNIST-gil 50, Ulju-gun, Ulsan 689-798, Republic of Korea.
E-mail: ykim@unist.ac.kr or hyunhko@unist.ac.kr
Received 3 March 2016; revised 23 April 2016; accepted 6 June 2016

aqueous and non-aqueous Na–air batteries have been studied; however, aqueous Na–air batteries have a fundamental advantage due to the formation of a highly soluble discharge product (sodium hydroxide).[21] Despite the great advantage of the aqueous Na–air battery, its rechargeability has not yet been demonstrated when using non-precious metal catalysts. Hayashi *et al.*[25] investigated only discharge properties of an aqueous Na–air cell using expensive Pt and Pd metals as electrocatalysts. In this work, we prepared an MGC air electrode by directly growing hierarchical urchin-shaped α-MnO_2 on a rGO-coated carbon microfiber without the use of a binder; this approach is completely different from the traditional blade coating methods via slurry and mechanical pressing methods. The direct growth of α-MnO_2 nanowires on a rGO-coated carbon microfiber provides efficient ion and electron transport and good mechanical adhesion of the active material to the carbon microfiber. By using the MGC air electrode, the assembled aqueous Na–air battery displays an excellent cycling stability, a low overpotential gap (0.7 V) and a high round-trip efficiency of 81%. Thus, we believe that our approach opens a new way to fabricate robust high-performance binder-free electrodes that can be utilized to fabricate cost-effective and large-scale energy storage devices, such as supercapacitors, metal–ion batteries, metal–air batteries and fuel cells.

MATERIALS AND METHODS

Synthesis of MGC electrode

The synthesis of urchin-shaped α-MnO_2 on a rGO-coated carbon microfiber was performed in two steps, which are discussed below in detail. We also propose a synthesis mechanism of the urchin-shaped MnO_2 on the carbon microfiber, which is discussed in the Supplementary Information.

Step 1: Preparation of the rGO-coated carbon microfiber

Graphene oxide (GO) was synthesized using a modified Hummers method reported by our group.[26] First, 0.05 g of GO was dispersed in 10 ml of water by sonication, followed by the addition of 500 µl of a polystyrene (PS) solution (Polysciences, Warrington, PA, USA) and continuously sonicated for 4 h. Subsequently, 2 ml of the above solution was transferred to a Teflon-lined stainless steel autoclave with piranha-treated 2 cm × 2 cm carbon microfiber (JNT20, JNTG, Gyeonggi, Korea). The entire reaction mixture was sonicated for 2 h, transferred to a hot air oven, and then heated at 160 °C for 12 h. After the reaction, the autoclave was allowed to cool naturally to room temperature. The obtained carbon microfiber was washed with water and ethanol to remove the impurities and dried in an oven at 60 °C for 4 h. After drying, the carbon microfiber was dipped in a toluene solution to etch the PS and dried again.

Step 2: Synthesis of urchin-shaped α-MnO_2 on the rGO-coated carbon microfiber

In a typical synthesis of the urchin-shaped MnO_2 on the rGO-coated carbon microfiber, 1.5 mmol $KMnO_4$ (Sigma Aldrich, St Louis, MO, USA) was dissolved in 2.5 mmol concentrated HCl (DaeJung Chemicals, Gyeonggi, Korea) and 15 ml of distilled water. The mixture was stirred vigorously for several minutes until a purple solution was formed. The rGO-coated carbon microfiber was then dipped in the above solution, and the entire reaction mixture was transferred to a Teflon-lined stainless steel autoclave, and heated in a hot air oven at 90 °C for 4 h. Subsequently, the oven temperature was increased to 140 °C and kept constant for 24 h. After the reaction, the autoclave was left to cool naturally to room temperature, and the carbon microfiber was removed. The obtained carbon microfiber was washed several times with water, and ethanol to remove the impurities, and dried in an oven at 60 °C for 3 h. In the other experiments, only the reaction time varied, but all other reaction conditions were identical.

Characterization

Powder X-ray diffraction (XRD) measurements were performed to analyze the phase formation of the material using a Bruker D8 diffractometer with a Cu-Kα radiation ($\lambda = 0.154$ nm) source over the 2θ range of 15–60°. The chemical bonding and functional groups were investigated by X-ray photoelectron spectrometry (XPS, K-alpha, Thermo Fisher, Waltham, MA, USA) and confocal Raman microscopy (alpha 300R, WITec, Ulm, Germany) with an excitation wavelength of 532 nm. The surface morphologies of the samples were examined by field emission scanning electron microscopy (SEM) (FE-SEM; Hitachi, Tokyo, Japan, S-4800) at 10 kV operating voltage. The sample was placed on the conductive carbon tapes, which were positioned on top of the field emission SEM stubs. The transmission electron microscopy (TEM) sample was prepared by cutting a small piece of electrode, ultrasonicating it in ethanol and placing droplets of the as-prepared sample from the ethanolic dispersion on a carbon-coated Cu grid (200 mesh); the droplets were subsequently left to dry. TEM and selected area electron diffraction analyses were performed using a JEOL JEM 2100 high-resolution transmission electron microscope, using an accelerating voltage of 200 kV. Energy-dispersive X-ray spectroscopy analysis was performed, and elemental maps were obtained with an INCA, Oxford Instruments system attached to the HR-TEM. BET surface areas were analyzed by nitrogen (N_2) adsorption at liquid N_2 temperatures with a Micromeritics ASAP 2020 nitrogen adsorption apparatus. All the samples were degassed at 120 °C for 12 h before the N_2 adsorption measurements.

Electrochemical characterization

To examine the electrocatalytic activity, rotating ring-disk electrode (RRDE) experiments were conducted using the catalysts as working electrodes, the Pt wire as the counter electrode and Hg/HgO as the reference electrode in an oxygen-saturated 0.1 M NaOH aqueous electrolyte. To prepare the catalyst ink, the catalyst and the conducting agent were mixed in a solution of 900 µl of ethanol and 100 µl of 5 wt% nafion (Sigma Aldrich). The total amount of catalyst (80%) with conducting agent (carbon black; Akzo Nobel Ketjenblack 600JD, 20%) was maintained at 10 mg. The resulting solution was ultrasonicated for 30 min to prepare a catalyst ink. Then, 6 µl of the catalyst ink was pipetted onto the 0.1256 cm^2 disk compartment of the ring-disk working electrode (platinum-glassy carbon ring-disk), which resulted in a 0.38 mg cm^{-2} loading of the catalyst. The electrochemical characterizations were performed using a Bipotentiostat (Iviumstat, Ivium Technologies, Eindhoven, Netherlands), and the RRDE was rotated at 1600 r.p.m. by an RRDE controller (ALS RRDE-3A). ORR polarization curves were obtained on the disk electrode during a cathodic sweep from +0.1 to −0.8 V (vs Hg/HgO) at 10 mV s^{-1}. The electrolyte was saturated by oxygen for the ORR while it was purged by nitrogen to measure the background currents. OER polarization curves were obtained for a voltage ranging from +0.35 to +0.8 V (vs Hg/HgO) at 10 mV s^{-1}. The polarization curves were obtained after confirming that the voltammograms did not change significantly during the initial 10 cycles. Polarization curves for 20 wt% Pt nanoparticles supported by carbon black (Pt/C; Premetek P10A200), rGO, MnO_2 flake and RuO_2 were also analyzed for comparison. The experimental conditions were kept the same as in the case of the MGC catalyst. The electron transfer number (n) was calculated using the following equation:[3]

$$n = 4\frac{I_d}{I_d + I_r/N}$$

where I_d is the disk current, I_r is the ring current and N is the current collection efficiency of the Pt ring, which was determined to be 0.41.

The MGC electrode without any binder or conductive additives was directly used as an air electrode in a built aqueous Na–air battery. For the negative electrode compartment design, metallic Na (Sigma Aldrich) was adhered on Ni foam and $NaCF_3SO_3$ (Sigma Aldrich) in a tetraethylene glycol dimethyl ether (TEGDME) solvent used as the anolyte. In the other compartment, the as-prepared MGC air electrode was attached to a Ti mesh as the current collector and a 0.1 M NaOH solution was utilized as the catholyte. The air electrode was left exposed to airflow. These two compartments were separated by a solid electrolyte NASICON ($Na_3Zr_2Si_2PO_{12}$) membrane; the electrochemical studies were conducted with a WBCS3000L, WonATech workstation (Seoul, Korea).

RESULTS AND DISCUSSION

Fabrication of MGC electrodes

Binder-free hierarchical micro- and nanostructured air electrodes were fabricated by directly growing urchin-shaped MnO_2 nanowires on a carbon microfiber coated with porous rGO films, as schematically shown in Figure 1a. Briefly, the carbon microfiber underwent a hydrothermal process to obtain a uniform coating of rGO and PS nanoparticle mixtures (Supplementary Figure S1a). Subsequently, the PS nanoparticles were selectively etched, resulting in the formation of porous rGO films on the carbon microfiber (Supplementary Figure S1b). Then, the rGO-coated carbon microfiber was kept in a $KMnO_4$ solution and subjected to another hydrothermal treatment, during which the reduction of Mn^{7+} to Mn^{4+} occurred, resulting in the formation of hierarchical air electrodes based on urchin-shaped MnO_2 nanowires on the rGO-coated carbon microfiber (Figures 1b–f). The key advantages of the hierarchical MGC paper as the air electrode in a Na–air battery include the following factors: (**1**) an efficient pathway for the diffusion of electrolyte and air provided by the hierarchical morphology of the urchin nanostructures on the porous microfiber mats; (**2**) the binder-free and direct growth of MnO_2 nanowires on the conductive support to obtain efficient electron transport; (**3**) large active sites provided by the urchin-shaped MnO_2 nanowires; and (**4**) the robust adhesion of MnO_2 nanowires on porous graphene films. Along with these benefits, we believe that the presence of rGO greatly improves the conductivity of the electrode. Compared with other conductive supports (such as Ni foam, Cu foil, Al foil and Ti mesh), carbon microfiber is economical, lightweight and highly porous (which is beneficial for air diffusion).

Figures 1b–e shows the SEM images of a hierarchical MGC electrode, which consists of hierarchical scales of a microfibrous network of carbon microfiber (Figure 1b), urchin microspheres on the microfibers (Figure 1c) and MnO_2 nanowires in the urchin microspheres (Figures 1d and e). The carbon microfibers with the rGO coating are uniformly covered with urchin-shaped microspheres (diameters of 5–10 μm), which are composed of radially oriented MnO_2 nanowires (diameters of 20–25 nm). A similar surface morphology was observed on the opposite side of the microfiber (Supplementary Figure S2), thus indicating the uniform growth of urchin-shaped MnO_2 nanowires on the rGO-coated carbon microfiber. The TEM analysis confirmed that the MnO_2 nanowires are highly crystalline (Figures 1g and h) with a growth direction along the (200) plane and an interplanar spacing of 0.49 nm, which is a characteristic plane of the α-phase of MnO_2 and is not found in other phases of MnO_2.[27] The elemental mapping of a MnO_2 nanowire indicated the presence of Mn and O elements (Figure 1i).

The growth mechanism of the urchin-shaped MnO_2 nanowires on the rGO-coated carbon microfibers can be explained by the bubble-template assembly of MnO_2 nanocrystals into a spherical shape and

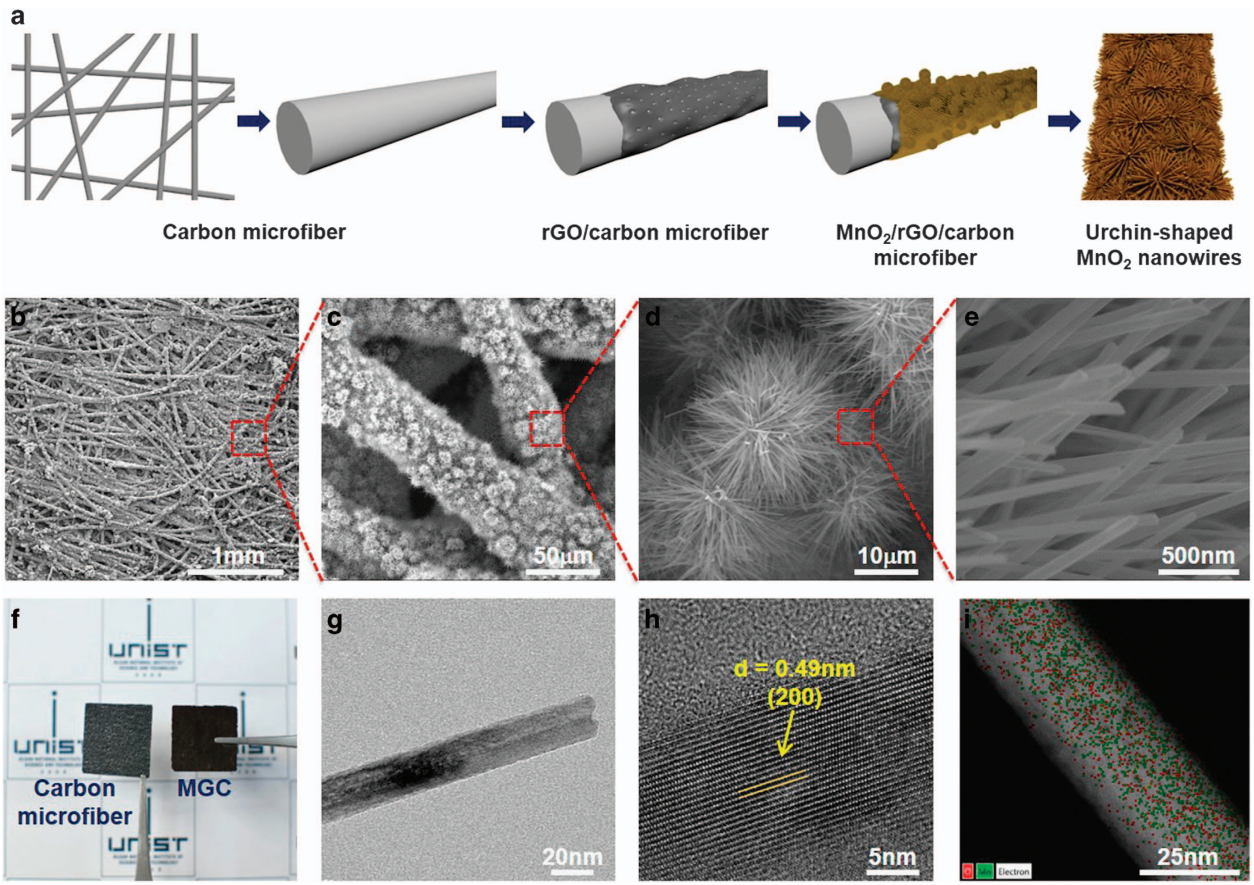

Figure 1 Synthetic scheme and morphological study of urchin-shaped α-MnO_2 nanowires on reduced graphene oxide-coated carbon microfiber (MGC) electrode. (**a**) Schematic illustration for the synthesis of the MGC electrode via the hydrothermal method. Scanning electron microscopy images of (**b**) the microfibrous network of the carbon microfiber, (**c**) the urchin-shaped microspheres on the carbon microfiber, (**d**) the urchin morphology of MnO_2 and (**e**) the high-magnification scanning electron microscopy image showing MnO_2 nanowires. (**f**) Photograph of the carbon microfiber and the MGC electrode. (**g**) TEM image of MnO_2 nanowires. (**h**) High-resolution TEM images showing the (200) lattice plane of MnO_2. (**i**) Elemental mapping on MnO_2 nanowires.

the subsequent growth of MnO_2 nanowires in the radial direction. rGO possesses unreduced surface functional groups, even after the hydrothermal treatment of GO and in the presence of HCl acid; the unreduced functional groups on the rGO sheets lead to the production of CO_2, CO and H_2 gases in the solution.[28,29] Then, the generated gas bubbles are trapped by the porous defect sites on the graphene surface and induce the assembly of MnO_2 nanocrystals at the liquid/gas interface as a consequence of the minimization of the interfacial energy (Supplementary Figure S3a). This assembly process occurs during the hydrothermal reduction of $KMnO_4$ into MnO_2 nanocrystals at 90 °C for 4 h. Notably, the assembly of MnO_2 nanocrystals into microspheres is not observed in non-porous rGO-coated carbon microfibers (Supplementary Figure S3b), thus indicating the critical role of porous rGO in the formation of the urchin-shaped MnO_2 microspheres. Finally, the spherically assembled MnO_2 nanocrystals grow into nanowires in the radial direction under specific growth conditions (140 °C for 24 h), which gives rise to the urchin-shaped MnO_2 nanowires. In this final process, the nanowire growth time critically affects the uniform formation of the urchin-shaped MnO_2 nanowires (Supplementary Figure S4). A shorter growth time (6 h) produces flake-shaped structures, whereas a growth time of 12 h leads to a mixed morphology of flakes and nanowires and a longer growth time (48 h) results in larger nanowires with urchin-like structures. The porous graphene structure on the carbon microfiber is an important factor for the formation of MnO_2 microspheres (Supplementary Figure S3a) and the further growth of uniform urchin-shaped MnO_2 nanowires (Figures 1b–e). On the carbon microfiber coated with non-porous graphene, a non-uniform coverage of spherical microstructures of MnO_2 nanoflakes was observed (Supplementary Figure S5). On the bare carbon microfiber without the graphene coating, only randomly entangled networks of MnO_2 nanowires were observed (Supplementary Figure S6).

Figure 2a shows the XRD pattern of an MGC electrode prepared by the hydrothermal method. All the marked XRD peaks are consistent with the standard JCPDS card of the α-phase MnO_2 (JCPDS No. 44-0141, space group *I4/m*), thus indicating the formation of the α-phase MnO_2 in the MGC electrode. The diffractogram can be indexed to the tetragonal structure with the crystal lattice parameters of $a = b = 0.97847$ and $c = 0.28630$ nm. The diffraction peak at $2\theta = 17.8°$ is also in good agreement with the HR-TEM result showing the characteristic (200) plane of the α-MnO_2 crystal structure. No impurity peaks were observed in the MGC diffractogram, except the peak at $2\theta \approx 26°$, which can be attributed to the rGO coating layer.[7] The chemical bonding state of the MGC electrode was investigated by Raman spectroscopy and XPS, as shown in Figures 2b–f. The Raman bands at 570 and 650 cm^{-1} can be ascribed to the Mn–O stretching vibration in the basal plane of the MnO_6 sheet and the symmetric stretching vibration Mn–O of the MnO_6 groups, respectively (Figure 2b).[30] In the Raman spectra of MGC, the D and G bands were not observed, thus confirming that the carbon microfiber is fully covered by the MnO_2 nanowires. The XPS survey scan in Figure 2c clearly shows the presence of the Mn, O and C elements in the sample. The Mn 2p XPS spectrum in Figure 2d shows two peaks at the binding energies of ~654 and ~642 eV, which can be ascribed to the Mn $2p_{3/2}$ and Mn $2p_{1/2}$ spin-orbital doublets in MnO_2, respectively.[31] In the O 1s XPS spectrum (Figure 2e), the major peak at 529.5 eV is attributed to the Mn–O bonding energy. The C 1s XPS spectrum of MGC (Figure 2f) shows a broad peak, which can be deconvoluted into three different peaks located at 284.1, 285.8 and ~288 eV, corresponding to the carbon bonds of C=C, C–O–C and carbonyl (C=O),

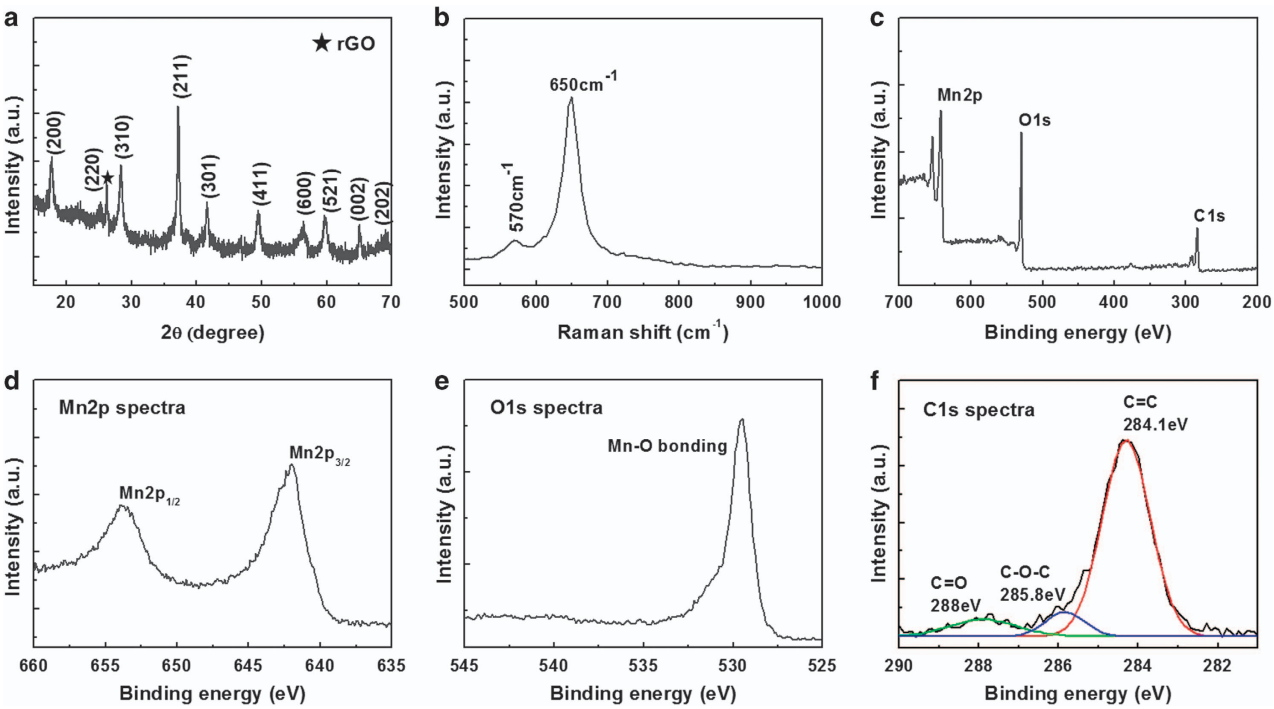

Figure 2 Phase characterization and chemical bonding analyses. (**a**) Powder XRD pattern of urchin-shaped α-MnO_2 nanowires on a reduced graphene oxide-coated carbon microfiber (MGC) electrode. XRD confirms the formation of the α-phase MnO_2. (**b**) Raman spectrum and (**c**) XPS survey scan of the MGC electrode. High-resolution XPS spectra of (**d**) Mn 2*p*, (**e**) O 1*s* and (**f**) C 1*s* for the MGC electrode. In **c**, the survey spectrum reveals the presence of the Mn, C and O elements in the MGC electrode. In **d**, the XPS peaks are assigned to the Mn $2p_{3/2}$ and Mn $2p_{1/2}$ binding energies. The spectrum in **e** confirms the presence of a metal oxide (Mn–O) bond. In **f**, the deconvoluted peaks were assigned to the C=C, C–O–C and C=O functional groups.

respectively. The presence of the carbon functional groups is mainly due to rGO. The Raman and XPS spectra of the rGO-coated carbon microfiber without the MnO_2 nanostructures reveal the reduced state of the rGO sheets on the carbon microfiber, which can be clearly recognized upon comparison with the Raman and XPS spectra of bare carbon paper. (Supplementary Figures S7 and S8; a detailed discussion is provided in the Supplementary Sections 3 and 4).

Electrocatalytic activity of MGC electrode for ORR and OER

In metal–air batteries, the bifunctional electrocatalyst is a crucial component in reducing the activation energy of both the ORR and the OER. To investigate the electrocatalytic ORR and OER activity of the MGC electrode, RRDE measurements in an O_2 saturated 0.1 M NaOH electrolyte solution at 1600 r.p.m. were conducted with a Hg/HgO reference electrode and compared with noble metal Pt/C, RuO_2, rGO and flake-shaped MnO_2 electrodes (Figure 3). The ORR polarization curve of a disk electrode shown in Figure 3a confirms the electrocatalytic activity of the prepared MGC electrode with an onset potential of −60 mV vs Hg/HgO, which was negative to that of the Pt/C electrode, but its activity sharply elevated with the increase of potential. At a potential of −0.8 V vs Hg/HgO, the MGC shows an ORR peak current density of −5.7 mA cm^{-2}, which is lower than that of Pt/C (−6.4 mA cm^{-2}). Compared with rGO and MnO_2 flakes, the MGC exhibits a more positive onset potential and a higher current density than the MnO_2 flake (−5.3 mA cm^{-2}) and rGO (−3.9 mA cm^{-2}). The higher catalytic activity of the MGC compared with the MnO_2 flake can be attributed to the ample active sites due to the hierarchical urchin morphology of the MGC.[32–35] The ORR polarization curves of the ring electrode in Figure 3b also support the ORR catalytic activity with a low-ring current for the MGC electrode, which suggests that the ORR process is mainly by a four-electron transfer pathway. The electron transfer number per oxygen molecule (n) for the ORR was determined by the disk current and the ring current of the ORR polarization curves (Figure 3c); the n value of MGC was calculated to be 3.96, suggesting a direct four-electron transfer pathway for the ORR, which is comparable to Pt/C ($n = 3.99$), but higher than MnO_2 flake ($n = 3.91$) and rGO ($n = 3.32$). The direct four-electron transfer process reveals that the electrocatalytic reaction involves a bidentate O_2 adsorption process, in which two oxygen atoms coordinate with Mn.[36] The proposed ORR steps (the reverse process is OER) using the MGC air electrode are discussed below:[14]

$$2MnO_2 + 2H_2O + 2e^- \leftrightarrow 2MnOOH + 2OH^- \quad (1)$$

$$O_2 + e^- \leftrightarrow O_{2,ads}{}^- \quad (2)$$

$$2MnOOH + O_{2,ads}{}^- + e^- \leftrightarrow 2MnO_2 + 2OH^-; \quad (3)$$

overall:

$$O_2 + 2H_2O + 4e^- \leftrightarrow 4OH^-(aq.) \quad (4)$$

Notably, MnO_2 crystallizes in the α-phase during the growth, which, in contrast to other phases of MnO_2, greatly facilitates the electrocatalytic process due to its crystal structure.[1,10] The crystal structure of α-MnO_2 consists of 2 × 2 tunnels formed by edge-sharing MnO_6 and corner sharing MnO_6 octahedra.[1] Owing to the tunnel size and the requirement to balance the negative charge, α-MnO_2 can accommodate positive ions in the tunnel cavities, thereby providing high feasibility for bidentate O_2 adsorption sites not only on the surface but also in the bulk material.[14] Depending on the proposed mechanism, for efficient electrocatalytic activity, a bifunctional

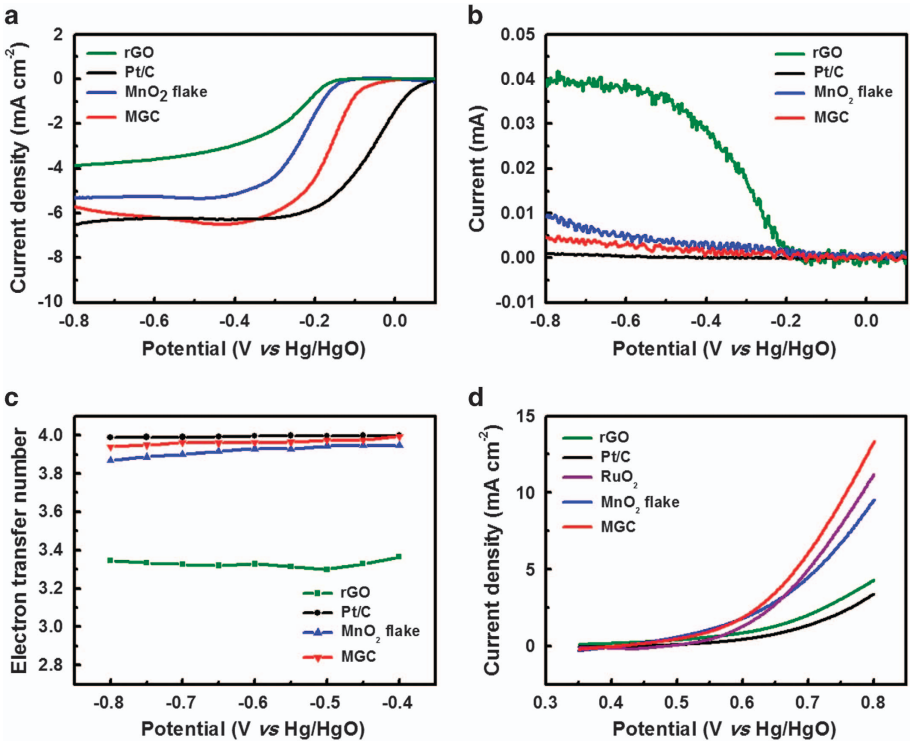

Figure 3 Electrocatalytic activity measurements of the urchin-shaped α-MnO_2 nanowires on a rGO-coated carbon microfiber (MGC) electrode. ORR polarization curves of (**a**), a disk and (**b**) a ring with rGO, Pt/C, MnO_2 flake and MGC electrode at 1600 r.p.m. in oxygen-saturated 0.1 M NaOH (scan rate; 10 mV s^{-1}). (**c**) Electron transfer number of rGO, Pt/C, MnO_2 flake and MGC electrode. (**d**) OER polarization curves of rGO, Pt/C, RuO_2, MnO_2 flake and MGC electrode at a rotating speed of 1600 r.p.m. with a scan rate of 10 mV s^{-1} in 0.1 M NaOH solution.

electrocatalyst should provide strong adsorption of electrolytic ions, excellent diffusion of electrolyte ions and air or oxygen to the catalyst surface, and good ionic and charge transfer capabilities. Remarkably, in our prepared MGC electrode, highly crystalline urchin-shaped MnO_2 meets all of the aforementioned essential criteria of a bifunctional electrocatalyst. In addition, the OER electrocatalytic activity of the MGC was compared with those of the noble metal Pt/C, RuO_2, rGO and MGC flakes (Figure 3d). The OER polarization curve confirms a higher OER electrocatalytic activity for MGC and shows the rapid increase in current above 0.65 V vs Hg/HgO associated with the OER and a low OER onset potential. The MGC displayed superior OER electrocatalytic activity (a highest OER peak current density and a lowest OER onset potential), which could be attributed to the hierarchically urchin morphology and rGO support. The cyclic stability of the MGC for the OER was also analyzed, as shown in Supplementary Figure S9, up to 30 cycles. Although the cyclic stability is not very high, it is still much better than the noble metal Pt/C in terms of current density observed after 30 cycles. These results corroborate the promising ORR and OER electrocatalytic activity of the MGC electrode, demonstrating that it can be used as a bifunctional electrocatalyst in a metal–air battery. The superior OER activity of MGC will also help reduce the electrode polarization in metal–air batteries.

Rechargeability of aqueous Na–air battery using MGC air electrode

An aqueous Na–air battery was built (see the schematic illustration in Figure 4a) using a binder-free MGC air electrode to investigate electrochemical properties such as the rate capability and cyclic stability. The redox processes concerning the aqueous Na–air battery can be described as follows:

$$\text{Cathode}: \quad 2H_2O + O_2 + 4e^- \leftrightarrow 4OH^-(\text{aq.}); \quad E^0 = +0.4 \text{ V vs SHE}$$

$$\text{Anode}: \quad Na^+ + e^- \leftrightarrow Na(s); \quad E^0 = -2.71 \text{ V vs SHE}$$

Normally, in a cell, the charge voltage is higher than the open circuit voltage, and the discharge voltage is lower than the open circuit voltage. The high-charge voltage could be attributed to the internal resistance, lower ionic conductivity than electronic conductivity, impurities in the electrode materials and varying ions diffusing from the surface to the bulk of the electrodes.[37] Such high-charge and low-discharge voltages lead to a low electrical energy efficiency of the cell, which is not beneficial for practical applications.[38] Figure 4b shows the constant current charge (associated with the OER) and discharge (associated with the ORR) at 15 mA g^{-1} of the aqueous Na–air battery using the MGC and Pt/C air electrodes for 25 h. When charging the cell with the MGC electrode, the charge voltage was 3.1 V and reached a value of only 3.59 V after ~ 10 h; thereafter, no increase in the potential was observed, but the potential reached 2.9 V during the discharge. Based on the theoretical redox potential of the cell (3.11 V),[23] the cell exhibits a charge overpotential (η_{chg}) of ~ 0.5 V and a discharge overpotential (η_{dis}) of ~ 0.2 V; hence, the charge–discharge potential gap (also called the overpotential gap) is only 0.7 V, and the round-trip efficiency is equal to 81%. The electrochemical performance of the Na–air cell built using the MGC air electrode is similar to that of the cell with the commercial Pt/C electrode and superior to that of the current Li–O_2 and non-aqueous Na–air cells (Supplementary Table 1).[22,37] Furthermore, we compared the rechargeable performance of cells based on the prepared MGC electrode with those based on the rGO-coated carbon microfiber, carbon black, and bare carbon microfiber electrodes, as shown in Figure 4c and Supplementary Figure S10a, and we observed the outstanding

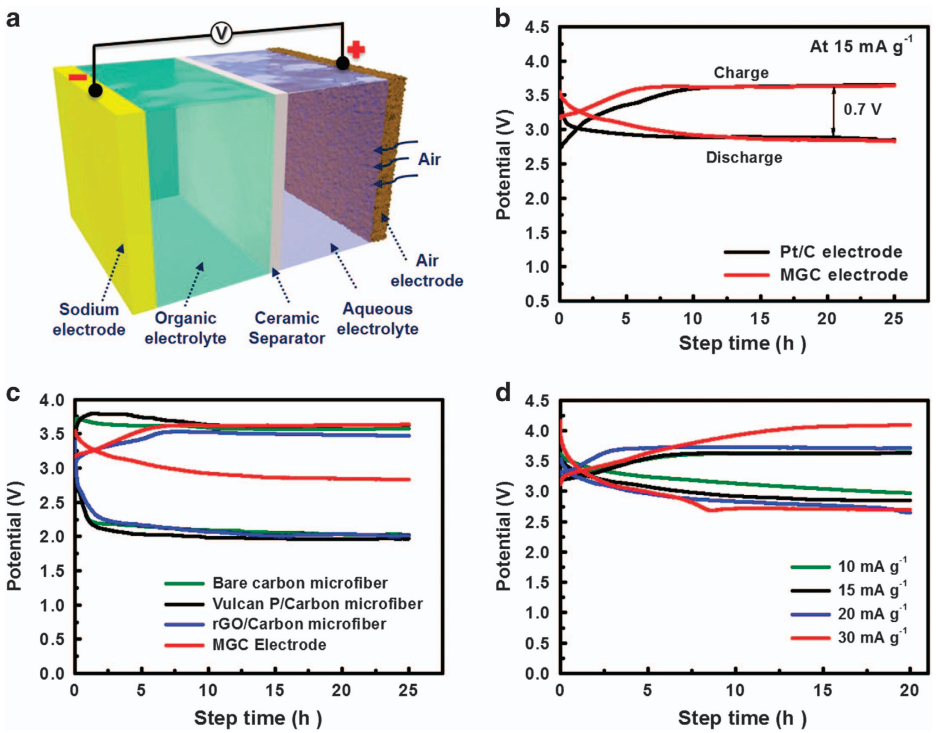

Figure 4 Schematic presentation and rechargeability demonstration of aqueous Na–air cell. (**a**) Design of the fabricated aqueous Na–air cell. (**b**) Charge (oxygen evolution reaction) and discharge (oxygen reduction reaction) profiles of the Pt/C and urchin-shaped α-MnO_2 nanowires on rGO-coated carbon microfiber (MGC) air electrodes at 15 mA g^{-1}. (**c**) Comparative charge–discharge profiles of bare carbon microfiber, carbon black, rGO-coated carbon microfiber and MGC at 15 mA g^{-1} as air electrodes. (**d**) Rate capability test at different rates ranging from 10 to 30 mA g^{-1} for an aqueous Na–air battery.

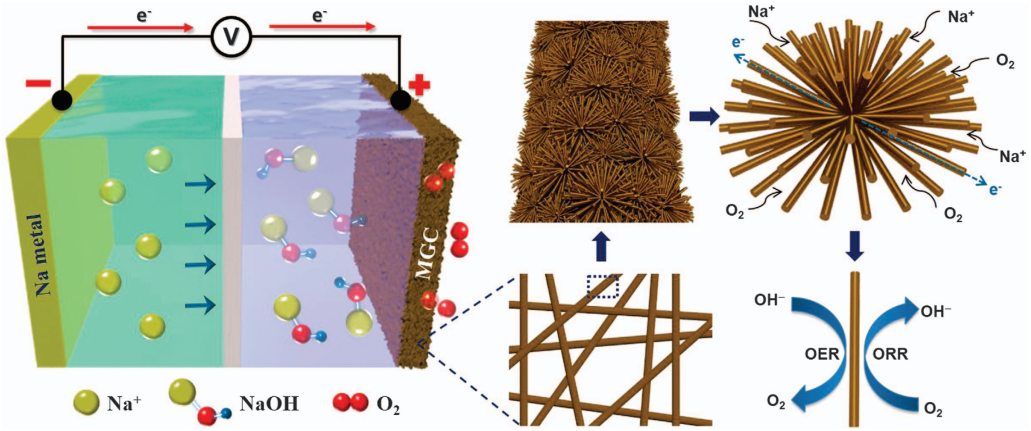

Figure 5 Mechanistic illustration of rechargeability of aqueous Na–air battery. Schematic presentation of the proposed mechanism for discharging (oxygen reduction reaction) and charging (oxygen evolution reaction) of a rechargeable Na–air battery using urchin-shaped α-MnO_2 nanowires on reduced graphene oxide-coated carbon microfiber air electrode. The urchin shape of the MnO_2 plays a crucial role during the electrolyte and air diffusion and, owing to the highly crystalline MnO_2, the electrode shows good ionic and charge transfer capabilities.

performance of the Na–air cell with the MGC electrode. The rate capability of the electrode was also examined by the charge–discharge of the cell at different current densities ranging from 10 to 30 mA g^{-1}, as shown in Figure 4d. The overpotential gap slightly increased with the increase in current density, which could be attributed to the fast diffusion of the electrolyte ions, indicating the good rate capability of the MGC electrode. Furthermore, the fabricated cell can give an uninterrupted maximum specific capacity of 1200 mA h g^{-1} when it is discharged at 30 mA g^{-1} for 40 h (Supplementary Figure S10b).

The excellent rechargeability of the Na–air cell with an MGC air electrode can be attributed to the urchin morphology of the MnO_2 and the superior electrocatalytic activity of the MGC. The mechanism responsible for the excellent performance of the urchin-shaped MGC electrode is illustrated in Figure 5. During the discharge, the electropositive Na metal oxidizes to become a Na^+ ion ($Na(s) \rightarrow Na^+ + e^-$) at the negative electrode and moves to the positive electrode through the electrolyte while the generated electrons transfer through the external circuit; during the recharge, the sodium is replated on the negative electrode. The generated electrons reduce the oxygen *via* the ORR process, and the reduced oxygen interacts with the sodium ions on the surface of the MGC air electrode. The MGC air electrode is composed of radially aligned highly crystalline MnO_2 nanowires with an urchin morphology. Owing to this morphology, the MnO_2 nanowires are assembled with continuous V-type channels, which have fully exposed active sites. The V-type channels in the air electrode facilitate the diffusion of the electrolyte, the contact of the air electrode with the electrolyte, and the transportation of Na^+ ions and electrons. As discussed above, a good electrocatalyst exhibits high adsorption of the electrolyte ions and excellent diffusion of air to the electrode surface. Thus, the formed V-type channels greatly enhance the electrocatalytic activity of the MGC electrode (facile ORRs and OERs) and make the cell rechargeable. Furthermore, the nanowire morphology minimizes the distance over, which the Na^+ ions have to diffuse during the redox processes and decreases the electrode polarization.[39–42] At the same time, highly crystalline MnO_2 nanowires are also sufficiently exposed for the O_2 diffusion and electron transport, greatly benefiting the ORR. Thus, owing to the urchin shape of the MnO_2, the MGC electrode exhibits an excellent rechargeable performance. To confirm our claim, the performance of urchin-shaped MnO_2 was compared with that of flake-shaped MnO_2 (SEM images of the flake-shaped MnO_2 are shown in Supplementary Figure S4a); the urchin-shaped MnO_2 exhibited a superior performance, as shown in Figure 6a, which is attributed to the higher surface area of the MGC air electrode (22 m^2 g^{-1}) compared with the MnO_2 flake electrode (15 m^2 g^{-1}) (Supplementary Figure S11). Moreover, we believe that the α-phase of MnO_2, as discussed above, and the rGO, which support the conductivity and hydrophilicity and the binder-free nature of the electrode, were also beneficial for the excellent performance of the aqueous Na–air cell.

The rechargeability of the MGC electrode was examined up to 20 cycles, and the charge–discharge profiles for different cycles are shown in Figure 6b. No significant potential drop was observed under continuous charge–discharge of the cell up to 1000 h (at a 15 mA g^{-1} current density). We also plotted the potential difference between the charge and discharge steps of the MGC electrode and found that there is only a slight increase in the overpotential gap (from 0.7 to 0.84 V) with the number of cycles (Figure 6c). In addition, the round-trip efficiency of the cell was calculated to be ~78%, from 81%, after 20 cycles (Figure 6c), thus indicating the excellent rechargeability of the aqueous Na–air battery with the urchin-shaped MnO_2 air electrode. The outstanding rechargeable performance of the MGC could be attributed to the rational design of the electrode (urchin morphology, rGO support and binder-free) and excellent electrocatalytic activity towards the ORR and OER. As discussed above, compared with Pt/C, the MGC exhibits a similar ORR activity and an improved OER activity, thereby leading to highly reversible redox processes that cause outstanding charge–discharge repeatability. By contrast, the robust nature of the MGC electrode may also contribute to the excellent rechargeability. The robust nature of the MGC was demonstrated by comparing SEM images, XRD patterns, and XPS spectra of the MGC electrode before and after the electrochemical charge–discharge experiments (Figure 6d and Supplementary Figure S12). No significant change was observed in the morphology of the MGC electrode even after 20 cycles (1000 h of charge–discharge at 15 mA g^{-1}), which indicates the superb adhesion of the active material to the current collector (Figure 6d). Furthermore, the α-phase of the MnO_2 was also retained after 20 charge–discharge cycles, as confirmed by XRD analysis (Supplementary Figure S12a). The diffraction peaks slightly shifted towards higher 2θ angles, which could be due to the strain caused inside the crystal structure of the transition metal oxides during the charge–discharge of the cell.[43] Along with the rGO and α-MnO_2 diffraction peaks, an additional peak at 22.5°, which is associated with

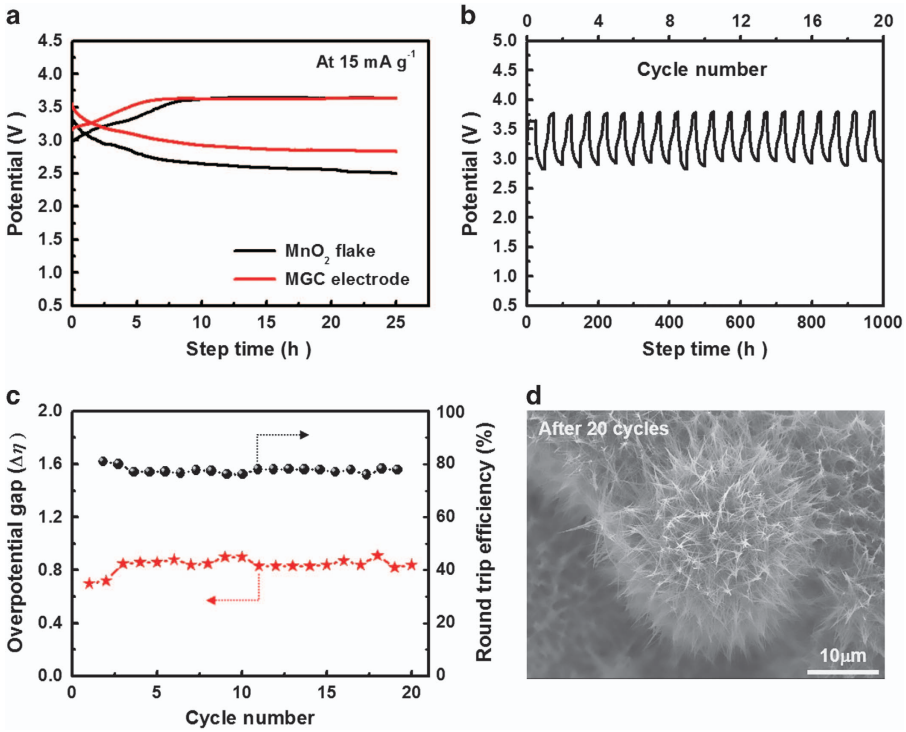

Figure 6 Performance and cyclic stability test of aqueous Na–air battery. (**a**) Charge–discharge profile of urchin-shaped and flake-shaped MnO_2 on rGO-coated carbon microfiber. (**b**) Voltage profiles up to 20 cycles for the rechargeable Na–air battery at a current density of 15 mA g^{-1}. (**c**) Overpotential gap ($\Delta\eta$) and round-trip efficiency (%) plotted against the number of cycles. (**d**) Scanning electron microscopy image of urchin-shaped α-MnO_2 nanowires on rGO-coated carbon microfiber air electrode after 20 cycles (1000 h).

hydrated sodium hydroxide (JCPDS No. 03-0089), was also observed. The XPS survey spectra of the MGC after 20 charge–discharge cycles indicate the presence of Mn, O, C and Na (Supplementary Figure S12b). The high-resolution XPS spectra of Mn 2p and O 1s show similar peaks (Supplementary Figure S12c and d); however, for C 1s, in contrast to the spectrum of the MGC electrode before the charge–discharge process, an additional peak appears at 289.4 eV (Supplementary Figure S12e), which could be assigned to the carboxyl group. In the high-resolution Na 1s XPS spectrum, the major peak at 1070 eV is attributed to metallic Na (Supplementary Figure S12f). In addition, we examined the stability of the solid NASICON electrolyte in an alkali solution by XRD before cycling and after electrochemical charge–discharge cycles, as shown in Supplementary Figure S13. No significant change in the diffractogram was observed for the NASICON before and after cycling, which proves the stability of the NASICON in an alkali solution.

CONCLUSION

In conclusion, urchin-shaped α-MnO_2 was grown on a rGO-coated current collector (carbon microfiber) via the hydrothermal method; the rechargeability of the aqueous Na–air battery was demonstrated for the first time using MGC as a bifunctional, binder-free and robust air electrode. The rechargeable performance of the aqueous Na–air battery using the MGC air electrode was compared with that of a battery using the noble metal Pt; the MGC air electrode showed a similar rechargeable performance to the Pt electrode, which is due to the urchin-shaped MnO_2 (the maximum diffusion of the electrolyte and air as well as the fast transport of ions and electrons), the α-phase of MnO_2, the excellent electrocatalytic activity, a high surface area, the rGO coating on the current collector and the binder-free and robust (adhesion between the electroactive material and the current collector) electrode. Additionally, the overpotential gap and round-trip efficiency were calculated to be 0.7 V and 81%, respectively. The fabricated cell exhibited an excellent rechargeability up to 20 cycles with a low overpotential gap and good round-trip efficiency. Our electrode fabrication strategy provides a cost-effective approach for addressing the high overpotential gap and low round-trip efficiency associated with metal–air batteries, thus opening a practical way to creating economical and large-scale energy storage devices for electric and hybrid electric vehicles. Furthermore, this strategy can be utilized to fabricate electrodes that can be used not only in metal–air batteries but also in metal–ion batteries, supercapacitors and fuel cells.

CONFLICT OF INTEREST

The authors declare no conflict of interest.

ACKNOWLEDGEMENTS

This work was supported by the National Research Foundation of Korea (NRF-2011-0014965, 2015R1A2A1A10054152), the Center for Advanced Soft-Electronics funded by the Ministry of Science, ICT and Future Planning as Global Frontier Project (2015M3A6A5065314), and the 2016 Research Fund (1.160004.01) of UNIST (Ulsan National Institute of Science and Technology).

1 Débart, A., Paterson, A. J., Bao, J. & Bruce, P. G. α-MnO_2 nanowires: a catalyst for the O_2 electrode in rechargeable lithium batteries. *Angew. Chem. Int. Ed. Engl.* **47**, 4521–4524 (2008).

2 Lim, H.-D., Song, H., Kim, J., Gwon, H., Bae, Y., Park, K. Y., Hong, J., Kim, H., Kim, T., Kim, Y. H., Lepró, X., Ovalle-Robles, R., Baughman, R. H. & Kang, K. Superior rechargeability and efficiency of lithium-oxygen batteries: hierarchical air electrode architecture combined with a soluble catalyst. *Angew. Chem. Int. Ed. Engl.* **126**, 4007–4012 (2014).

3 Zhang, J., Zhao, Z., Xia, Z. & Dai, L. A metal-free bifunctional electrocatalyst for oxygen reduction and oxygen evolution reactions. *Nat. Nanotechnol.* **10**, 444–452 (2015).
4 Peng, Z., Freunberger, S. A., Chen, Y. & Bruce, P. G. A reversible and higher-rate Li-O_2 battery. *Science* **337**, 563–566 (2012).
5 Wang, C., Daimon, H., Lee, Y., Kim, J. & Sun, S. Synthesis of monodisperse Pt nanocubes and their enhanced catalysis for oxygen reduction. *J. Am. Chem. Soc.* **129**, 6974–6975 (2007).
6 Cheng, F. & Chen, J. Metal-air batteries: from oxygen reduction electrochemistry to cathode catalysts. *Chem. Soc. Rev.* **41**, 2172–2192 (2012).
7 Cao, Y., Wei, Z., He, J., Zang, J., Zang, Q., Zheng, M. & Dong, Q. α-MnO_2 nanorods grown *in situ* on graphene as catalysts for Li-O_2 batteries with excellent electrochemical performance. *Energy Environ. Sci.* **5**, 9765–9768 (2012).
8 Yang, Y., Shi, M., Li, Y.-S. & Fu, Z.-W. MnO_2-graphene composite air electrode for rechargeable Li-air batteries. *J. Electrochem. Soc.* **159**, A1917–A1921 (2012).
9 Luo, W.-B., Chou, S.-L., Jia-Zhao, W., Zhai, Y.-C. & Liu, H.-K. A facile approach to synthesize stable CNTs@MnO electrocatalyst for high energy lithium oxygen batteries. *Sci. Rep.* **5**, 8012 (2015).
10 Jang, H., Zahoor, A., Jeon, J. S., Kim, P., Lee, Y. S. & Nahm, K. S. Sea urchin shaped α-MnO_2/RuO_2 mixed oxides nanostructure as promising electrocatalyst for lithium–oxygen battery. *J. Electrochem. Soc.* **162**, A300–A307 (2015).
11 Liu, W., Sun, Q., Yang, Y., Xie, J.-Y. & Fu, Z.-W. An enhanced electrochemical performance of a sodium-air battery with graphene nanosheets as air electrode catalysts. *Chem. Commun.* **49**, 1951–1953 (2013).
12 Jian, Z., Chen, Y., Li, F., Zhang, T., Liu, C. & Zhou, H. High capacity Na–O_2 batteries with carbon nanotube paper as binder-free air cathode. *J. Power Sources* **251**, 466–469 (2014).
13 Li, Y., Yadegari, H., Li, X., Banis, M. N., Li, R. & Sun, X. Superior catalytic activity of nitrogen-doped graphene cathodes for high energy capacity sodium-air batteries. *Chem. Commun.* **49**, 11731–11733 (2013).
14 Meng, Y., Song, W., Huang, H., Ren, Z., Chen, S.-Y. & Suib, S. L. Structure–property relationship of bifunctional MnO_2 nanostructures: highly efficient, ultra-stable electrochemical water oxidation and oxygen reduction reaction catalysts identified in alkaline media. *J. Am. Chem. Soc.* **136**, 11452–11464 (2014).
15 Xiao, W., Wang, D. & Lou, X. W. Shape-controlled synthesis of MnO_2 nanostructures with enhanced electrocatalytic activity for oxygen reduction. *J. Phys. Chem. C* **114**, 1694–1700 (2010).
16 Li, Y., Wang, J., Li, X., Geng, D., Li, R. & Sun, X. Superior energy capacity of graphene nanosheets for a nonaqueous lithium-oxygen battery. *Chem. Commun.* **47**, 9438–9440 (2011).
17 Yoo, E., Nakamura, J. & Zhou, H. N-doped graphene nanosheets for Li-air fuel cells under acidic conditions. *Energy Environ. Sci.* **5**, 6928–6932 (2012).
18 Zhou, X., Qiao, J., Yang, L. & Zhang, J. A review of graphene-based nanostructural materials for both catalyst supports and metal-free catalysts in PEM fuel cell oxygen reduction reactions. *Adv. Mater.* **4**, 1301523 (2014).
19 Ha, D.-H., Islam, M. A. & Robinson, R. D. Binder-free and carbon-free nanoparticle batteries: a method for nanoparticle electrodes without polymeric binders or carbon black. *Nano Lett.* **12**, 5122–5130 (2012).
20 Hartmann, P., Bender, C. L., Vračar, M., Dürr, A. K., Garsuch, A., Janek, J. & Adelhelm, P. A rechargeable room-temperature sodium superoxide (NaO_2) battery. *Nat. Mater.* **12**, 228–232 (2013).
21 Ha, S., Kim, J.-K., Choi, A., Kim, Y. & Lee, K. T. Sodium–metal halide and sodium–air batteries. *Chem. Phys. Chem.* **15**, 1971–1982 (2014).
22 Das, S. K., Lau, S. & Archer, L. A. Sodium-oxygen batteries: a new class of metal-air batteries. *J. Mater. Chem. A* **2**, 12623–12629 (2014).
23 Kuratani, K., Uemura, N., Senoh, H., Takeshita, H. T. & Kiyobayashi, T. Conductivity, viscosity and density of $MClO_4$ (M = Li and Na) dissolved in propylene carbonate and γ-butyrolactone at high concentrations. *J. Power Sources* **223**, 175–182 (2013).
24 Park, S. I., Gocheva, I., Okada, S. & Yamaki, J.-I. Electrochemical properties of $NaTi_2(PO_4)_3$ anode for rechargeable aqueous sodium-ion batteries. *J. Electrochem. Soc.* **158**, A1067–A1070 (2011).
25 Hayashi, K., Shima, K. & Sugiyama, F. A mixed aqueous/aprotic sodium/air cell using a NASICON ceramic separator. *J. Electrochem. Soc.* **160**, A1467–A1472 (2013).
26 Shin, Y. E., Sa, Y. J., Park, S., Lee, J., Shin, K. H., Joo, S. H. & Ko, H. An ice-templated, pH-tunable self-assembly route to hierarchically porous graphene nanoscroll networks. *Nanoscale* **6**, 9734–9741 (2014).
27 Zhang, J., Li, Y., Wang, L., Zhang, C. & He, H. Catalytic oxidation of formaldehyde over manganese oxides with different crystal structures. *Catal. Sci. Technol.* **5**, 2305–2313 (2015).
28 Wang, R., Higgins, D. C., Hoque, M. A., Lee, D., Hassan, F. & Chen, Z. Controlled growth of platinum nanowire arrays on sulfur doped graphene as high performance electrocatalyst. *Sci. Rep.* **3**, 2431 (2013).
29 Cao, J., Wang, Y., Xiao, P., Chen, Y., Zhou, Y., Ouyang, J.-H. & Jia, D. Hollow graphene spheres self-assembled from graphene oxide sheets by a one-step hydrothermal process. *Carbon* **56**, 389–391 (2013).
30 Xia, H., Wang, Y., Lin, J. & Lu, L. Hydrothermal synthesis of MnO_2/CNT nanocomposite with a CNT core/porous MnO_2 sheath hierarchy architecture for supercapacitors. *Nanoscale Res. Lett.* **7**, 1–10 (2012).
31 Reddy, A. L. M., Shaijumon, M. M., Gowda, S. R. & Ajayan, P. M. Coaxial MnO_2/carbon nanotube array electrodes for high-performance lithium batteries. *Nano Lett.* **9**, 1002–1006 (2009).
32 Morozan, A., Jégou, P., Campidelli, S., Palacin, S. & Jousselme, B. Relationship between polypyrrole morphology and electrochemical activity towards oxygen reduction reaction. *Chem. Commun.* **48**, 4627–4629 (2012).
33 Zhang, L., Lee, K. C. & Zhang, J. J. Effect of synthetic reducing agents on morphology and ORR activity of carbon-supported nano-Pd-Co alloy electrocatalysts. *Electrochim. Acta* **52**, 3088–3094 (2007).
34 Vankayala, K., Kancharlapalli, S. & Srinivasan, S. Morphology dependent oxygen reduction activity of titanium carbide: bulk vs nanowires. *Phys. Chem. Chem. Phys.* **15**, 8744–8751 (2013).
35 Kukunuri, S., Krishnan, M. R. & Sampath, S. The effect of structural dimensionality on the electrocatalytic properties of the nickel selenide phase. *Phys. Chem. Chem. Phys.* **17**, 23448–23459 (2015).
36 Wang, Z.-L., Xu, D., Xu, J.-J. & Zhang, X.-B. Oxygen electrocatalysts in metal-air batteries: from aqueous to nonaqueous electrolytes. *Chem. Soc. Rev.* **43**, 7746–7786 (2014).
37 Park, J.-K (ed.). The basic of battery chemistry. in *Principles and Applications of Lithium Secondary Batteries*, 9–19 (Wiley-VCH Verlag GmbH & Co. KGaA, 2012).
38 Girishkumar, G., McCloskey, B., Luntz, A. C., Swanson, S. & Wilcke, W. Lithium – air battery: promise and challenges. *J. Phys. Chem. Lett.* **1**, 2193–2203 (2010).
39 Liu, B., Zhang, J., Wang, X., Chen, G., Chen, D., Zhou, C. & Shen, G. Hierarchical three-dimensional $ZnCo_2O_4$ nanowire arrays/carbon cloth anodes for a novel class of high-performance flexible lithium-ion batteries. *Nano Lett.* **12**, 3005–3011 (2012).
40 Wang, Y. G., Li, H. Q. & Xia, Y. Y. Ordered whiskerlike polyaniline grown on the surface of mesoporous carbon and its electrochemical capacitance performance. *Adv. Mater.* **18**, 2619–2623 (2006).
41 Liu, B., Wang, X., Liu, B., Wang, Q., Tan, D., Song, W., Hou, X., Chen, D. & Shen, G. Advanced rechargeable lithium-ion batteries based on bendable $ZnCo_2O_4$-urchins-on-carbon-fibers electrodes. *Nano Res.* **6**, 525–534 (2013).
42 Cheng, F., Zhao, J., Song, W., Li, C., Ma, H., Chen, J. & Shen, P. Facile controlled synthesis of MnO_2 nanostructures of novel shapes and their application in batteries. *Inorg. Chem.* **45**, 2038–2044 (2006).
43 Khan, Z. & Qureshi, M. Tantalum doped $BaZrO_3$ for efficient photocatalytic hydrogengeneration by water splitting. *Catal. Commun.* **28**, 82–85 (2012).

Supplementary Information accompanies the paper on the NPG Asia Materials website (http://www.nature.com/am)